magnetochemistry

MDPI

Article

Structural, Morphological and Ferroelectric Properties of Sr-Cd Co-Doped Nickel Ferrite for Energy Storage Devices

Huda A. Alburaih [1], Muhammad Ahsan ul Haq [2], Abdul Jabbar [3], Atiq ur Rehman [4,*], Amel Laref [5], Mohamed Musa Saad Hasb Elkhalig [6] and Naveed Ahmad Noor [2]

[1] Department of Physics, College of Science, Princess Nourah Bint Abdulrahman University, Riyadh 11671, Saudi Arabia; haalburaih@gmail.com
[2] Department of Physics, Riphah International University Lahore Campus, Lahore 53700, Pakistan; ahsanulhaq168@gmail.com (M.A.u.H.); naveed.noor@riphah.edu.pk (N.A.N.)
[3] Department of Physics, University of Lahore, Lahore 53700, Pakistan; ajp2361@gmail.com
[4] Department of Physics, Emerson University Multan, Multan 60000, Pakistan
[5] Department of Physics and Astronomy, College of Science, King Saud University, Riyadh 11451, Saudi Arabia; larefamel@yahoo.com
[6] Department of Physics, College of Science, Qassim University, Buridah 51452, Saudi Arabia; 141261@qu.edu.sa
* Correspondence: atiqurrehman8337@gmail.com

Abstract: Ferroelectric materials, renowned for their capacity to demonstrate spontaneous electric polarization reversible through an external electric field, are essential in numerous technological applications owing to their distinctive characteristics. For this, a series of spinel Sr-Cd co-doped nickel ferrite nanomaterials $Cd_{0.5-x}Sr_xNi_{0.5}Fe_2O_4$ (x = 0.0, 0.1, 0.2 and 0.3) were prepared through the standard sol-gel auto combustion method The XRD patterns showed that the prepared samples have a cubic spinel structure. The crystallite sizes of the samples vary from 29 to 40 nm. The morphology of prepared samples showed uniformly distributed spheres. Magnetic properties showed the soft magnetic nature of the prepared ferrites. The ferroelectric study revealed that Sr-Cd substituted ferrites exhibited the elliptical nature of ferroelectric loops at normal room temperature. The maximum polarization has been achieved at x = 0.3. The understanding of current and voltage (I–V) showed a slowly decreasing tendency of leakage current on both sides symmetrically against the increasing Sr content. The conductivity of the prepared spinel increases as a function of higher Sr doping. The real part of dielectric constant increases with increasing frequency. The materials show large elliptical loops indicating high asymmetric ferroelectric energy storage capability.

Keywords: spinel ferrites; Sr-Cd doping; cubic structure; ferroelectric analysis; conductivity

check for updates

Citation: Alburaih, H.A.; ul Haq, M.A.; Jabbar, A.; ur Rehman, A.; Laref, A.; Saad Hasb Elkhalig, M.M.; Noor, N.A. Structural, Morphological and Ferroelectric Properties of Sr-Cd Co-Doped Nickel Ferrite for Energy Storage Devices. *Magnetochemistry* **2024**, *10*, 48. https://doi.org/10.3390/magnetochemistry10070048

Academic Editor: Carlos J. Gomez

Received: 2 April 2024
Revised: 26 June 2024
Accepted: 29 June 2024
Published: 2 July 2024

Copyright: © 2024 by the authors. Licensee MDPI, Basel, Switzerland. This article is an open access article distributed under the terms and conditions of the Creative Commons Attribution (CC BY) license (https://creativecommons.org/licenses/by/4.0/).

1. Introduction

The overuse of fossil fuels endangers the environment and hastens the depletion of nonrenewable energy supplies [1,2]. This critical situation may be addressed by updating low-cost, renewable, and environmentally friendly sustainable energy and storage technologies [3]. Developing devices that store energy, such as solar cells, supercapacitors (SCs), fuel cells and energy obtained from sustainable sources are two essential strategies for resolving the world's energy challenge in the future [4]. A lot of attention has been paid to the inexpensive materials for electrodes utilized in SCs. Biomass energy and renewable energy technology have made significant contributions to ensuring humanity's energy future. The rising usage of renewable energy sources will demand a significantly higher capacity for charge storage. As a result, developing effective energy storage technologies has become ever more vital [5–8].

Ferrites are the principal chemical elements of ferric oxides, especially Fe_2O_3 and FeO, which are sometimes partially substituted by oxides that contain other transition metals,

which develop as powder or ceramic bodies that exhibit ferromagnetic qualities [9]. The ferrites are classified into three distinct categories based on their crystalline structure: spinel MFe_2O_4, garnet $M_3Fe_5O_{12}$, and hexagonal $MFe_{12}O_{19}$ [10]. Ferrites are attracting substantial interest and are still the topic of innumerable investigations owing to their potential application in high-density data storage mediums, magneto refrigeration systems, microwave magnetized devices, transducer cores, catalysis, and many other applications [11]. An ordinary spinel catalyst contains the chemical formula AB_2X_4, where "A" signifies a divalent ion, "B" denotes a trivalent ion, and "X" corresponds to an oxide ion [12]. Spinel ferrites have been at the forefront of nanotechnology and nanoscience in recent years due to other remarkable characteristics, such as their nanoscale size as well as super-paramagnetic behavior [13–15].

Ferrites are excellent materials for a variety of industrial (sensors, photoelectric devices, photo catalysis, magnetic pigments, energy storage devices, controlled signal transformation, batteries) and biomedical (drug delivery, MRI, tissue, bio-magnetic separation, tumor treatment) applications [16–20]. The production technique, additive calcination, and substitution procedure all affect the ferrite's structure and physical characteristics [21]. The optical, dielectric, electrical, and magnetic features of nanoscale $NiFe_2O_4$ can be improved and controlled by doping with ions of transition metals, like Co^{2+}, Zn^{2+}, Ni^{2+} [17,22–24]. Doping spinel ferrite with transition metal ions alters the distribution of cations between the octahedral (B) and tetrahedral (A) sites, resulting in refined magnetic characteristics. Moreover, the doped ions may alter the energy of the grain boundaries, functioning as a catalyst for grain growth [25].

Spinel ferrites make excellent substitute materials for single-metal oxides owing to their immense impact on magnetic and electrical fields. The nanocrystalline ferrites category contains nickel ferrite ($NiFe_2O_4$) and is considered an appealing material [26]. $NiFe_2O_4$ corresponds to the cubic spinel structural compounds family, and its inverse spinel geometry comprises Fe^{3+} ions at the A sites and Ni^{2+} ions at the B sites with equal distribution [27,28]. Magnetic nanomaterials have lately gained popularity precisely because of their new material characteristics that differ dramatically from those found in their bulk counterparts [29]. Ni-based materials have received substantial investigation and are currently regarded as excellent future electrode materials for pseudo capacitors due to their exceptional specific capacitance, remarkable chemical and thermal stability, and lower price when compared to other transition metal oxides (TMOs) [30].

Nickel ferrite is a sort of soft ferrite that forms an inverse spinel via Ni^{2+} ions in the B sub-lattice and Fe^{3+} ions in both A and B sub-lattices. Because of their ability to form square bonds, Cd^{2+} and Sr^{2+} ions favor tetrahedral locations. Introducing diamagnetic Cd^{2+} and Sr^{2+} ions into the Ni ferrite lattice influences the crystal's local shape, converting it to a mixed spinel [31]. It additionally has the potential to improve ferroelectric characteristics such as polarisation, saturation, and magnetization. Because Cd^{2+} ions are intermittent, they may produce cationic deficiencies at higher sintering temperatures. At the same time, discrepancies in ionic radii may cause crystal deformation, causing a strain in the structure and substantial spin canting. This interaction between cationic vacancies and ionic radius variations will result in a considerable shift in the value of the observed magnetic moment, suggesting further analysis [32–34].

The literature on Sr-Cd co-doped nickel ferrite systems is scarce. We systematically studied the effects of Cd^{+2} and Sr^{+2} ion doping on the structural and morphological, magnetic and ferroelectric characteristics of nickel ferrite. We have implemented the sol-gel auto combustion technique with an organic fuel mixture of glycine and urea. When compared to alternative synthesis processes such as vapor phase deposition, ball milling, etc., the sol-gel auto combustion approach ensured phase purity and particle size uniformity, as well as a lower number of imperfections [35,36]. XRD, SEM, magnetic and ferroelectric characterization of the samples were performed to evaluate the structural changes created in the samples and the morphology of nanostructures and P-E loops at normal ambient temperature. It additionally exists that trivalent ion replacement improves stor-

age capacity. As an outcome, it becomes very exciting to substitute divalent co-doped ferrite ($Cd_{0.5-x}Sr_xNi_{0.5}Fe_2O_4$) and investigate its structural, morphological, magnetic and ferroelectric properties for prospective use in energy storage devices.

2. Experimental Section

2.1. Materials

Urea $CO(NH_2)_2$, glycine [NH_2CH_2COOH], Nickel nitrate [$Ni(NO_3)_2.H_2O$], Strontium nitrate [$Sr(NO_3)_2$] Cadmium nitrate [$Cd(NO_3)_2$], and Iron nitrate nonahydrate [$Fe(NO_3)_3.9H_2O$] were purchased from Sigma-Aldrich (Taufkirchen, Germany) with listed purity of 88.9%.

2.2. Material Synthesis

Sol-gel auto combustion was employed to fabricate the spinel ferrites $Cd_{0.5-x}Sr_xNi_{0.5}Fe_2O_4$ with (x = 0.0, 0.1, 0.2 and 0.3). The process of making ferrites involved combining urea [CH_4N_2O] and glycine [NH_2CH_2COOH] as the fuel agents with analytical-grade nickel nitrate [$Ni(NO_3)_2.6H_2O$], strontium nitrate [$Sr(NO_3)_2$] cadmium nitrate [$Cd(NO_3)_2$], and iron nitrate hexahydrate [$Fe(NO_3)_3.9H_2O$]. The stoichiometric values of the aforementioned chemicals were taken in separate beakers, and prior to combining all the components of a sample, the components were first dispersed individually in 50 mL deionized water for different values of x. The solution was stirred (50 rpm) while being heated at 80 °C and then burned until it turned into ash using a self-assisting burning technique. This process turned the solution into a gel. The pH of the solution has been maintained at 7. The burnt powder was then sintered for 4 h at 1200 °C to obtain single phase spinel ferrites. The sintered powder was further refined using mortar and piston. The refined powder thus obtained was used for X-ray diffraction using Cu-kα X-ray diffractometer (Rigaku Miniflex-II, Neu-Isenburg, Germany) with 1.54 Å wavelength. SEM images of the prepared samples were taken using (Hitachi-SU1510, Tokyo, Japan). Similarly, M-H loops were obtained using Lakhshore-7407 and P-E loops using measured at 300 K using 9 V driving voltages for PZT/LSM. The 0.8 g powdered sample $Cd_{0.5-x}Sr_xNi_{0.5}Fe_2O_4$ at x = 0.0, and 0.3 were turned into pellets of 1mm thickness using 40 kN force for 2 min and subsequently dielectric measurements have been made using R&S ZVA 50 VNA model in the frequency range 1 to 6 GHz.

3. Results and Discussion

3.1. XRD Analysis

The study of patterns obtained from XRD reveals the development of a single-phase compound exhibiting a cubic arrangement and the lattice parameter "a" for each specimen has been determined (Table 1). The crystal size (D) was determined from the XRD peak widening of the (220) peak utilizing Debye-Scherer's formula [37]. Figure 1 displays the XRD patterns of $Cd_{0.5-x}Sr_xNi_{0.5}Fe_2O_4$. According to the JCPDS# 01-074-2081, the XRD peaks for various amounts of x, i.e., (x = 0.0, 0.1, 0.2 and 0.3), for $Cd_{0.5-x}Sr_xNi_{0.5}Fe_2O_4$ at 2θ values of 30.29°, 35.68°, 47.46°, 53.81°, 57.37 °, 63.0° and 71.50° with (220), (311), (331), (422), (511), (440) and (620) planes have been observed (Figure 1a). The diffraction patterns demonstrate that when Sr content increases, the peak location for (220) shifts continually towards greater angles (Figure 1b).

Table 1. Structural parameters calculated from X-ray diffractometer.

Concentration (*x*)	Crystallite Size (D_p) (nm)	d-Spacing (Å)	Lattice Parameter '*a*' (Å)	Unit Cell Volume (10^6 pm^3)	X-ray Density (ρ_x) (g/cm^3)	Dislocation Dendity $\delta = 1/D^2$
$Cd_{0.5}$ $Sr_{0.0}$ $Ni_{0.5}Fe_2O_4$	29.67	1.5270	4.319	80.57	5.65	0.001136
$Cd_{0.4}$ $Sr_{0.1}$ $Ni_{0.5}Fe_2O_4$	35.42	1.5736	4.450	88.12	5.12	0.000797
$Cd_{0.3}$ $Sr_{0.2}$ $Ni_{0.5}Fe_2O_4$	38.05	1.6256	4.597	97.14	4.96	0.000691
$Cd_{0.2}$ $Sr_{0.3}$ $Ni_{0.5}Fe_2O_4$	39.93	1.7464	4.9395	120.5	4.66	0.000627

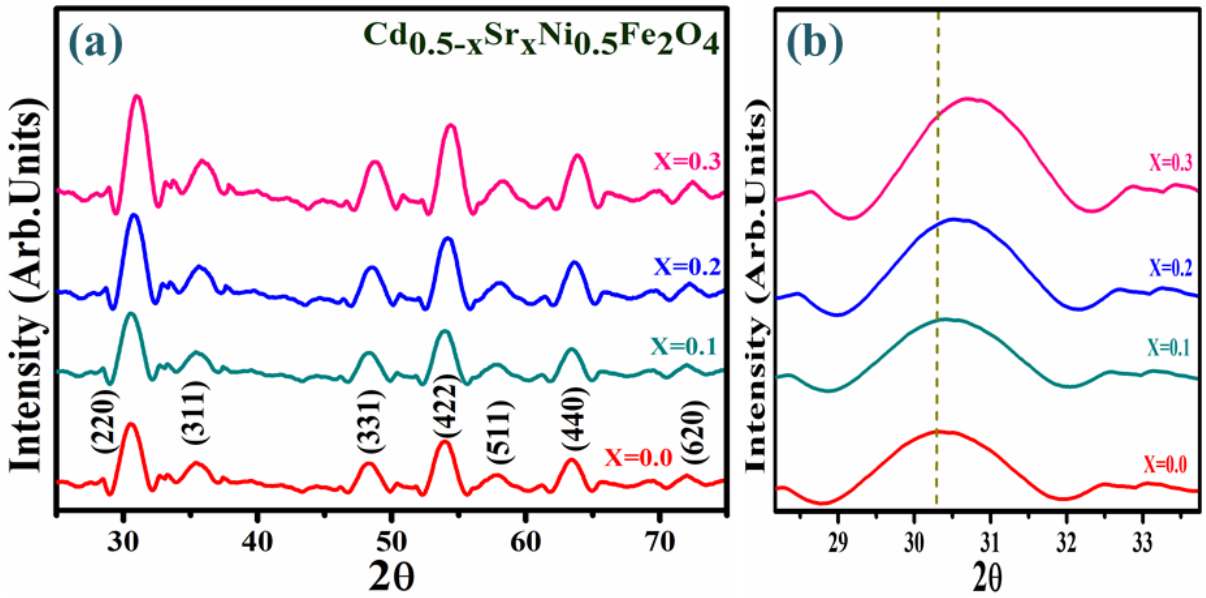


Figure 1. (**a**) XRD pattern of $Cd_{0.5-x}Sr_xNi_{0.5}Fe_2O_4$ (where x = 0.0, 0.1, 0.2 and 0.3) (**b**) enlarged view of (220) peak.

The determination of crystallite size for high-intensity peak (220) has been done using Scherrer's formula [37];

$$D = \frac{0.9\lambda}{\beta cos\theta} \quad (1)$$

The Bragg angle "θ", FWHM "β", and wavelength of the X-rays "λ" emitted from the "Cu" target are all given in the equation above. Whereas the following formula was used to compute the samples lattice parameter "a" [38]:

$$a = d \times \sqrt{h^2 + k^2 + l^2} \quad (2)$$

The Miller indices are represented by the letters "hkl" in the equation above, while the letter "d" represents the Bragg-law distance between the planes. Additionally, the following equation was used to determine the X-rays density "ρ_x" and dislocation density "δ" [39].

$$\rho_x = \frac{Z \times M}{N_A \times V} \quad (3)$$

$$\delta = \frac{1}{D^2} \quad (4)$$

The aforementioned equation uses the variables "M" for molecular weight, "N_A" for Avogadro number (6.022×10^{23} atm mol^{-1}), "V" for the volume of the unit cell, and "Z" for molecules/unit cell.

Table 1 shows a substantial rise in the lattice parameter when the Sr^{2+} concentrations in nickel ferrite increase. Higher values for d-spacing have been achieved due to greater ionic radii of Sr^{2+} than Cd^{2+}, which ultimately resulted in higher lattice parameter with doping. The widening of diffraction peaks is due to the tiny size of the produced particles. The size of the particles increased as the material composition and lattice constant increased. Cd^{2+} has an atomic radius of 0.97Å while Sr^{2+} has an atomic radius of 1.12 Å; subsequently, Cd^{2+} has a larger crystalline size than Sr^{2+} [37,40]. Higher values of lattice parameter resulted in achieving higher unit cell volume and lower X-ray density for co-doped samples. Dislocation density decreased due to increase in crystallite size.

3.2. Scanning Electron Microscopy (SEM)

The morphology of synthesized $NiFe_2O_4$ with different concentrations of Sr^{2+} and Cd^{2+} are depicted in Figure 2. The synthesized samples $Cd_{0.5-x}Sr_xNi_{0.5}Fe_2O_4$ with x = 0.0 and 0.1 exhibited a uniform distribution with spherical grains morphology appearing; furthermore, cracks are quite visible in SEM images. As the substitution of Sr^{2+} is increased formation of nanoplates start to form, and finally, at x = 0.3, nanoplates are clearly visible with larger and smaller grains distributed at random due to the agglomeration of tiny particles. It is also observed that when Sr^{2+} substitution increases, then the size of particles increases. Their porous nature was not significantly changed by the substitution of Sr^{2+} from their topological view. From Image J software, the average grain size was calculated, and it came out to be 9.64 µm, 9.89 µm, 11.1 µm, and 14.1 µm for x = 0.0, 0.1, 0.2, and 0.3 respectively.

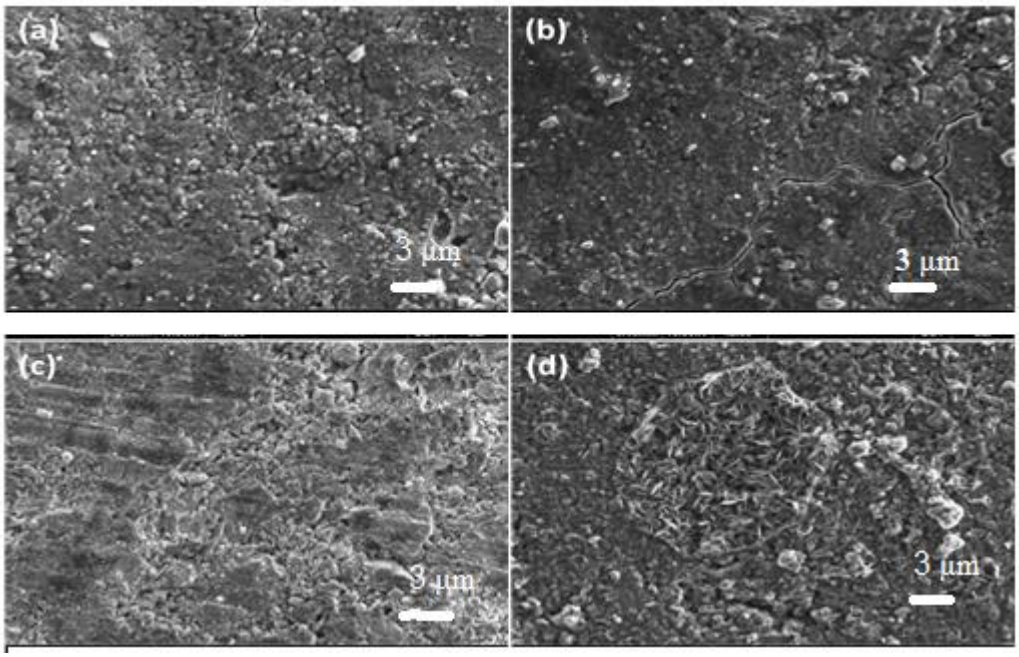


Figure 2. SEM images of $Cd_{0.5-x}Sr_xNi_{0.5}Fe_2O_4$ where (**a**) x = 0.0 (**b**) x = 0.1 (**c**) x = 0.2 and (**d**) x = 0.3.

3.3. Magnetic Properties

Figure 3 depicts magnetization profiles for $Cd_{0.5-x}Sr_xNi_{0.5}Fe_2O_4$ (with x = 0.0, 0.1, 0.2, and 0.3) along with implemented magnetic fields ranging from (+10.5 kOe to −10.5 kOe). Table 2 illustrates the computed values for fundamental magnetization characteristics, including saturation magnetization (M_s), magnetic remanence (M_r), and magnetic coercivity (H_c), based on the given M-H loops. The annealing procedures, grain development, chemical nature, and magneto-crystalline anisotropic field all have a significant influence in forming these loops [41]. Narrow S-shaped loops demonstrate the soft magnetic features of all manufactured spinel ferrites. Ferrites that possess this magnetic flexibility may be helpful in EM-absorbing substances, dielectric resonators, and monolayer chip inductors. Notably,

they are also beneficial in the assimilation of fluoride ions from consumed water [42,43]. It is widely accepted that a material's porosity increases coercivity while decreasing particle size. The size of particles corresponds oppositely, whereas porosity correlates directly to magnetized coercivity [44]. This is readily apparent when the value of x grows (i.e., x = 0.2, 0.3), whereby porosity and coercivity improve and particle size reduces. The M-H loop of the supplied sample suggests the ferrite possesses soft ferromagnetic nature with a small coercivity (<1000 Oe) [45]. It demonstrates that just a tiny magnetism needed to be created in order to eliminate magnetism from the supplied samples, revealing the soft magnetized behavior of $Cd_{0.5-x}Sr_xNi_{0.5}Fe_2O_4$. Insufficient coercivity values are ideal for magnetically safeguarding, EMI suppression, microwave instruments, and other critical armed forces and security infrastructure [46].

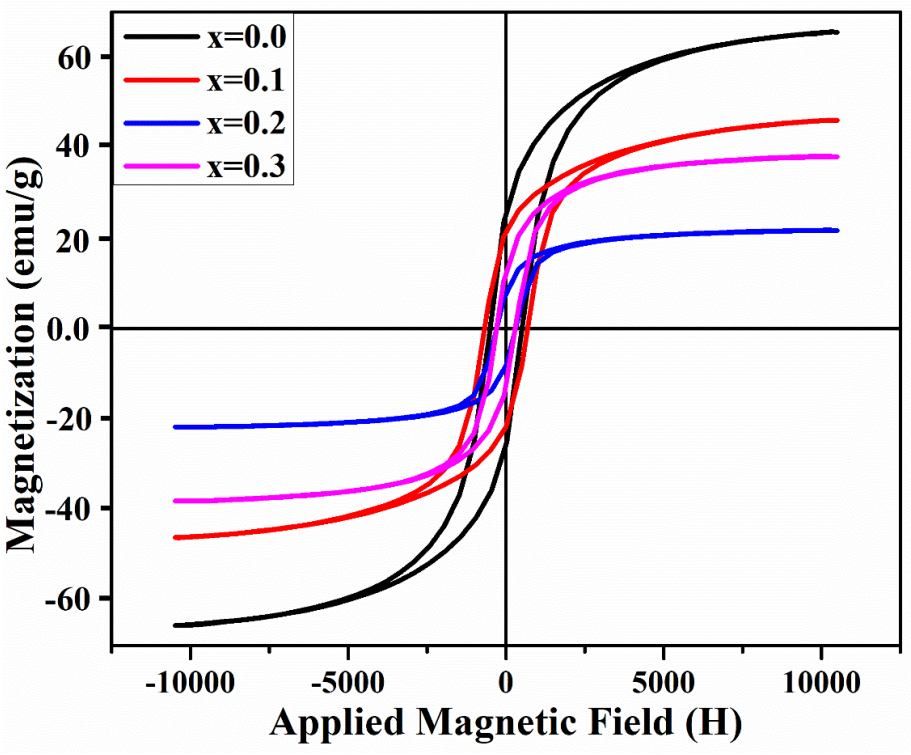


Figure 3. Hysteresis loop for $Cd_{0.5-x}Sr_xNi_{0.5}Fe_2O_4$ where x = 0.0, 0.1, 0.2 and 0.3.

Table 2. Magnetic parameters saturation magnetization (M_s), magnetic remanence (M_r), squareness ration (M_r/M_s), magnetic moment (n_B), magnetic coercivity (H_c), anisotropy constant (K), and anistropic field (H_k).

X	M_s emu/g ±0.01	M_r emu/g ±0.01	M_r/M_s	n_B (μ_B)	H_c Oe ±0.01	K $ergg^{-1}$	H_k (10^8)
0.0	65.58	25.16	0.38	3.076448	504	34,429.5	8.75
0.1	46.10	21.28	0.46	2.137851	681	32702.19	11.82
0.2	21.80	7.73	0.35	1.003151	297	6744.375	5.15
0.3	38.16	12.12	0.31	1.735477	295	11,726.25	5.12

As the quantity of Sr^{2+} increases, the saturation magnetization reduces in comparison to the un-doped sample. This phenomenon is mostly due to the decreasing strength of ferromagnetic interactions, as growing quantities of Fe^{3+} exhibiting elevated spin transform into Fe^{2+} with a comparatively low magnetic dipole moment [47]. The following greater saturation magnetization ensures that the manufactured ferrites may be easily removed

from aqueous dispersion using a magnetic field from the exterior. Additionally, magnetized remanence improves with Sr^{2+} replacements ranging from 7.73 emu/g to 25.16 emu/g. The squareness fraction ranges from 0.32 to 0.46, indicating that the manufactured material contains a single magnetized domain [48].

The magnetic moment (n_B) of $Cd_{0.5-x}Sr_xNi_{0.5}Fe_2O_4$ ferrites was calculated by using Equation (5) and outcomes are tabulated in table [49].

$$n_B(\mu_B) = \frac{M \times Ms}{5585} \quad (5)$$

Here, Molecular weight of samples is represented by 'M' and saturation magnetization is denoted by 'M_s'.

Anisotropic constant (K) and Anisotropic field (H_k) was calculated by using the Equations (6) and (7) respectively [50].

$$K = \frac{Hc \times Ms}{0.96} \quad (6)$$

$$H_K = \frac{2K}{\mu_o Ms} \quad (7)$$

Here, Coercivity is denoted by 'H_C' while the value of $\mu_o = 4\pi \times 10^{-7}$ H/m.

The Table 2 demonstrates that as dopant concentration increases, the value of anisotropic constant (K) and anisotropic field (H_k) reduces rather than being constant, indicating that the material is anisotropic. The lowering numbers enable the substance softer to magnetize in the prospective of the easiest direction. The coercivity exhibits inverse relationship with the size of the grains. The number of grain boundaries rises with grain size, making it challenging to arrange the domains. So, the coercivity of $Cd_{0.5-x}Sr_xNi_{0.5}Fe_2O_4$ nanoparticles decreases as grain size increases with Sr^{2+} injection [51].

3.4. Ferroelectric Analysis

Ferroelectricity is the key characteristic of these materials that have modernized the electronic realm. The phenomenon of ferroelectricity can easily be analyzed by polarization-electric field (P-E) hysteresis loop. Figure 4 demonstrated the P-E loops for the as-synthesized compositions recorded at 30 V. The elliptical nature observed in the P-E loops of the given ferrite system is indicative of hysteresis in the ferroelectric material. Hysteresis denotes a delay or lag in the response of the material when the electric field is applied or removed. The elliptical shape of the loop implies that the polarization of the material does not precisely track the applied electric field but instead retains a certain level of memory or residual polarization. The formation of an elliptical loop, rather than a perfect circle, suggests that the polarization reversal in the material lacks complete symmetry. This implies that the material may not switch back and forth with perfect balance, indicating some asymmetry in its switching behavior. Additionally, elliptical loops may also signal the occurrence of ferroelectric fatigue. Ferroelectric fatigue is a phenomenon wherein the material's switching characteristics degrade over repeated cycles of polarization reversal. In essence, the asymmetry in loop shape or any changes observed over time may be indicative of the material undergoing fatigue, potentially impacting its long-term stability. The area under the curve for PE loops is indicative of the energy loss during the polarization process. An elliptical loop indicates a particular dissipation pattern, interestingly low energy losses as compared to other shapes. In FeRAM elliptical loops shows the faster response time that benefits faster read/write operations from the memory. They are also beneficial for multifunctional devices such as energy harvesting devices where both mechanical and electric responses are crucial.

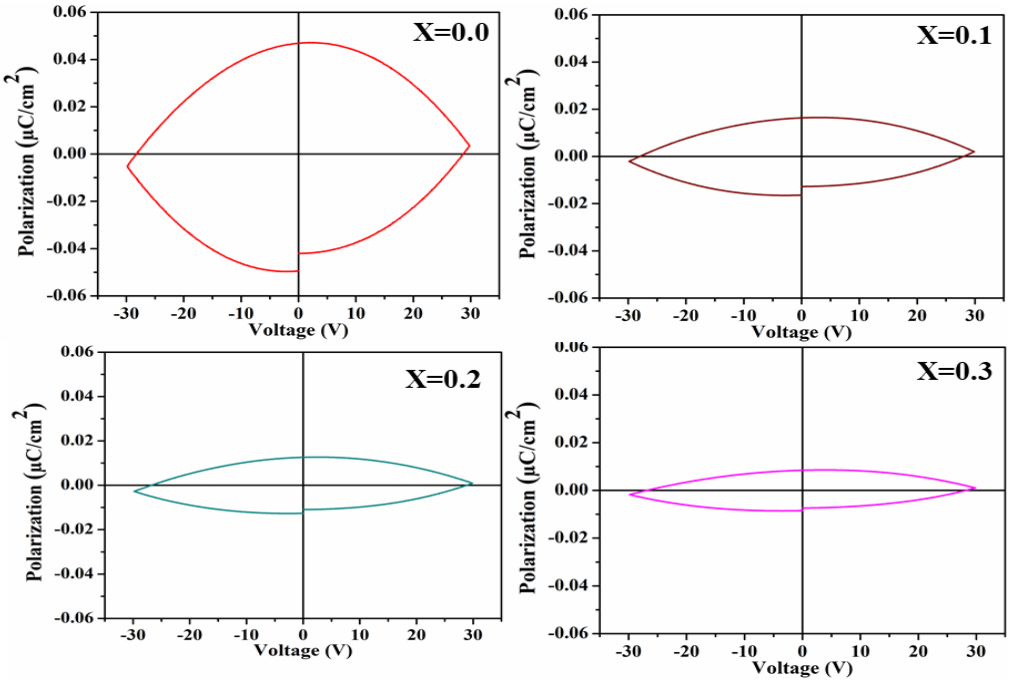


Figure 4. Ferroelectric behavior of $Cd_{0.5-x}Sr_xNi_{0.5}Fe_2O_4$ (where x = 0.0, 0.1, 0.2 and 0.3) respectively.

The P-E loops incorporated that the polarization exhibits a linear dielectric behavior. Such conduct is evident from the perceived increasing trend of polarization along with the electric field strength, which also assures the ferroelectric nature of the relevant samples. Ferroelectric analyses of Cd-Sr co-doped nickel ferrite nanoparticles $Cd_{0.5-x}Sr_xNi_{0.5}Fe_2O_4$ (x = 0.0, 0.1, 0.2 and 0.3) are represented by P-E plots at 30 V (Figure 4). As the applied electric field increases, the polarization in the material develops and dipoles align in the direction of the applied field. When the dipoles have reached the saturation level, the applied field begins to fall, resulting in a decrease in polarization. Nearly similar phenomena occur with negative electric fields. As a result, the highest coercivity value of 29.9 V/cm for $Cd_{0.5}Ni_{0.5}Fe_2O_4$ uniform P–E loop was obtained. The values of the coercive electric field for $Cd_{0.5-x}Sr_xNi_{0.5}Fe_2O_4$ (where x = 0.0, 0.1, 0.2 and 0.3, respectively) are given in Table 3. The coercivity value varies between 28 to 30V/cm with the rise in the concentration amount of doped Sr^{2+}.

Table 3. Coercive Electric Field (E_c), Recoverable Energy Density (W_R) and Energy Loss Density (W_L), Total Energy Density (W_T).

Contents X	E_c (KV/cm) ±0.02	W_R (J/cm^3)	W_L (J/cm^3)	W_T (J/cm^3)	Efficiency (η)
$Cd_{0.5}Sr_{0.0}Ni_{0.5}Fe_2O_4$	0.02999	0.12	1.965	2.0844	5.75
$Cd_{0.4}Sr_{0.1}Ni_{0.5}Fe_2O_4$	0.02802	0.426	1.045	1.471	28.95
$Cd_{0.3}Sr_{0.2}Ni_{0.5}Fe_2O_4$	0.02889	0.0578	0.0876	0.1454	39.73
$Cd_{0.2}Sr_{0.3}Ni_{0.5}Fe_2O_4$	0.02822	0.0734	0.0549	0.1282	57.20

P-E loops revealed an open-mouth structured for all samples. This is basically due to the conducting behaviour of these materials resulting in high leakage current. The high leakage current is mainly due to oxygen vacancies or voids in the prepared spinel ferrite. The P–E loop obtained in this case represents a lossy conductor type, possibly due to the large value of the leakage current [52,53]. The increase in the doping amount of Sr^{2+} ions on lattice sites has increased the P-E loop area, which may be due to the

increasing conducting behaviour of materials that leads to the rise in electrical leakage current. $Cd_{0.5}Ni_{0.5}Fe_2O_4$ displayed the lowest P–E loop area and the lowest leakage current. Increasing the content of Sr^{2+}, host ions remarkably increased the ferroelectric nature of $Cd_{0.5-x}Sr_xNi_{0.5}Fe_2O_4$. Saturation polarization was maximum for the highest doped sample (x = 0.30). This is because the dopant (Sr and Cd) ions had higher electrical responses than the host ions (Fe and Ni). Also, the structural changes improved the ferroelectric properties of the doped materials [54,55]. The values of maximum polarization (P_m) and remnant polarization (P_r) against varying values of Cd^{2+} and Sr^{2+} phase fractions has been shown in Figure 5. A decreasing trend of Pm, as well as Pr, was perceived with the increasing Sr_2O_3 phase fractions contributing low surface area offered by the relatively large particle size trapping numerous charge carriers [51]. With substitution, the uniform distribution of electric dipoles decreases. The simultaneous decrease in P_r and P_m in doped $NiFe_2O_4$ confirms short-range ordering, indicating ferroelectric phase stability. Saturation polarization increased with increasing Sr^{2+} content. Higher saturation polarization of the materials increases their energy storage capacity and makes them good candidates for use in energy storage devices. Properties like optical, electric and non-linear optics response for multi-layered capacitors LCD and storage devices can potentially be altered by altering the ferroelectric behaviors of the material, and a Cd^{2+} and Sr^{2+} doped material has potential use for such applications.

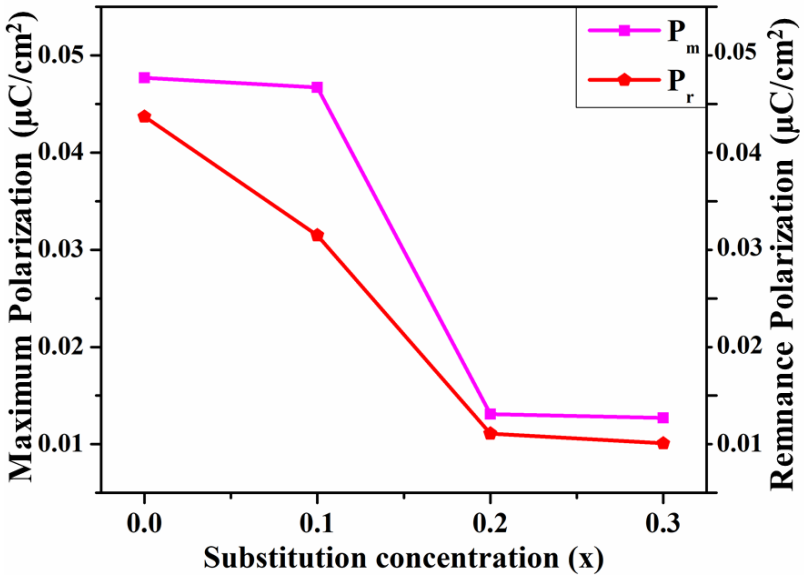


Figure 5. Maximum Polarization (P_m), and Remnance Polarization (P_r) of $Cd_{0.5-x}Sr_xNi_{0.5}Fe_2O_4$ (where x = 0.0, 0.1, 0.2 and 0.3) respectively.

The values of recoverable energy density (W_R), energy loss density (W_L) and total energy density (W_T) and Coercive Electric Field (E_c) for $Cd_{0.5-x}Sr_xNi_{0.5}Fe_2O_4$ (where x = 0.0, 0.1, 0.2 and 0.3), respectively at 30 V are tabulated in Table 3. Energy density can be efficiently calculated through P-E loops. Energy loss density (W_L) can be worked out by the area covered by P-E loops, whereas; plotting of the area enclosed by the discharge curve gives the value of recoverable energy density (W_R). By summarizing the values of W_L and W_R, one can determine the value of storage energy density (W_S). The values of W_L, W_R and W_S can be calculated by using Equation (8)–(10), respectively;

$$W_T = P_m P_r \quad (8)$$

$$W_R = (P_m - P_r)E_c \quad (9)$$

$$W_L = W_T - W_R \quad (10)$$

For x = 0.3, the variation of W_R and W_S clearly illustrates the enhanced recoverable energy density. These P-E loops also help to figure out the energy storage efficiency (η) of the material and can be calculated by using Equation (11) [56].

$$\eta = W_R/(W_R + W_L) \times 100\% \quad (11)$$

The efficiency of a prepared series of samples is depicted in Figure 6. The lowest efficiency has been achieved for x = 0.0. It was discovered that efficiency increased with increasing Sr^{2+} content. It is clear from the above equation that the value of efficiency (η) increased as W_R increased. This W_R value is associated with the region confined by the discharge curve and polarization axis.

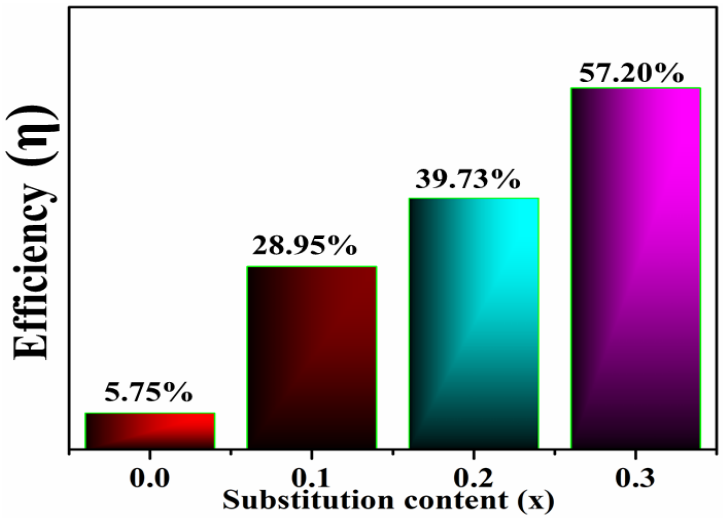


Figure 6. % Efficiency of $Cd_{0.5-x}Sr_xNi_{0.5}Fe_2O_4$ (where x = 0.0, 0.1, 0.2 and 0.3) respectively.

The current versus voltage (I–V) curves have been keenly analyzed for the as-synthesized samples. The plotted I–V graph is displayed in Figure 7. The leakage current exhibited symmetric trends for both the positive and negative sides of the applied field. A decreasing trend of leakage current had been perceived with the increasing Sr^{2+} phase fractions. The maximum current value was determined for the sample with concentration at x = 0.30. The leakage current moved symmetrically along the positive as well as negative boundaries of the practical field. With increasing Sr^{2+} substitution, a decreasing trend in leakage current was found.

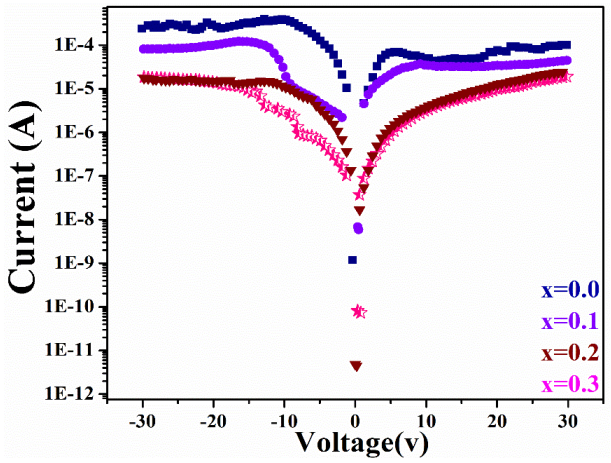


Figure 7. I–V characteristics of $Cd_{0.5-x}Sr_xNi_{0.5}Fe_2O_4$ (where x = 0.0, 0.1, 0.2 and 0.3) respectively.

3.5. Dielectric Response

The dielectric characteristics are crucial as they could be beneficial in understanding the dielectric energy storage behavior of the prepared materials. The real and imaginary parts of the permittivity against increasing frequency in the range 1 to 6 GHz has been shown in the Figure 8 for undoped and doped sample (x = 0.3). The curves show that the real part of the permittivity which is indicative of the dielectric energy stored in the material has a higher value and increases with increasing frequency. This means that the dielectric polarization for the given material increases at high frequency. The imaginary part of dielectric constant does not show much variation with increasing frequency. This is indicative that the ferrite material dielectric losses have not increased with increasing energy. The real part of permittivity shows higher values for doped sample (x = 0.3) as compared to undoped sample.

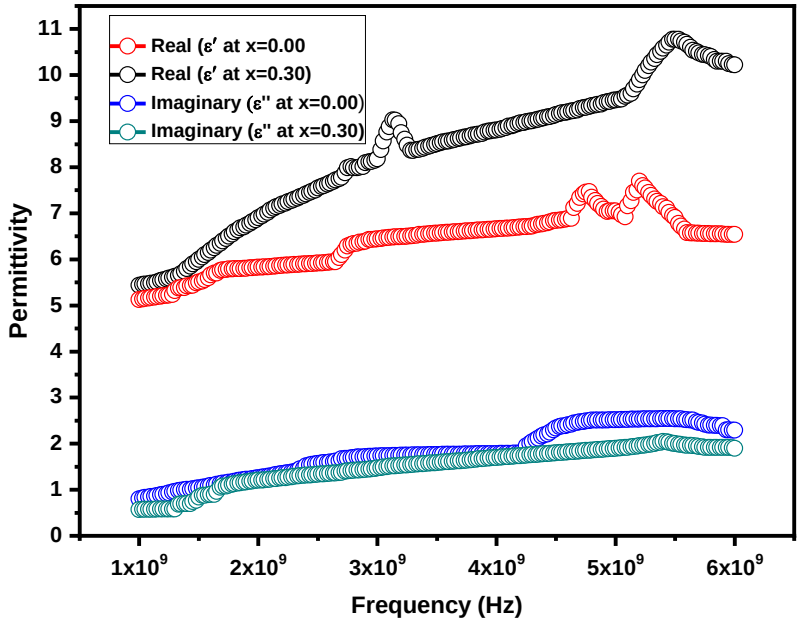


Figure 8. Real (ε') and imaginary (ε'') part of dielectric constant for undoped and doped (x = 0.3) samples.

4. Conclusions

In this work, the sol-gel auto combustion process was effectively affianced for producing $Cd_{0.5-x}Sr_xNi_{0.5}Fe_2O_4$ (x = 0.0, 0.1, 0.2 and 0.3). A systematic study of structural, morphological and ferroelectric effects of Sr-Cd doped NFO was utilized. The XRD peaks of all the samples indicate a spinel cubic structure with a highly crystalline nature. SEM analysis revealed the presence of cracks and oblong particles with a decrease in their average size. Magnetic parameters with S-shaped loops showed typical spinel ferrite response. P-E loops were consistent with every single sample accepted the normal room temperature ferroelectric nature, and the loop has a maximum value of P_m for x = 0.3. The P_m and P_r graph shows linearly decreasing trend with Sr-Cd substitution. W_R and W_L both increase with increasing values of substitution contents and is maximum at x = 0.3. The I–V graph shows the declining trend of leakage current observed with the increasing Sr substitution. The conductivity of these materials is maximum for maximum substitution of Sr and minimum substitution of Cd. The prepared samples show high real dielectric constant for doped sample. These materials are very useful and efficient for energy storage devices due to their characteristics.

Author Contributions: Conceptualization: A.u.R. and H.A.A.; Methodology: A.J. and A.L.; Software: A.L. and M.M.S.H.E.; Validation: M.A.u.H.; Formal Analysis: A.J.; Investigation: M.A.u.H.; Resources: A.u.R.; Data Curation: A.L. and N.A.N.; Writing Original Draft: H.A.A.; Supervision: A.u.R.; Review

& Editing: M.M.S.H.E. and N.A.N. All authors have read and agreed to the published version of the manuscript.

Funding: Researchers Supporting Project (Grant No. PNURSP2024R70), Princess Nourah Bint Abdulrahman University.

Institutional Review Board Statement: Not applicable.

Informed Consent Statement: Not applicable.

Data Availability Statement: No new data were created or analyzed in this study. Data sharing is not applicable to this article.

Acknowledgments: The authors express their gratitude to Princess Nourah Bint Abdulrahman University.

Conflicts of Interest: The authors declare that no conflict of interest is involved in the current study.

References

1. Ramzan, M.; Raza, S.A.; Usman, M.; Sharma, G.D.; Iqbal, H.A. Environmental cost of non-renewable energy and economic progress: Do ICT and financial development mitigate some burden? *J. Clean. Prod.* **2022**, *333*, 130066. [CrossRef]
2. Belhadj, H.; Messaoudi, Y.; Khelladi, M.R.; Azizi, A. A facile synthesis of metal ferrites (MFe_2O_4, M = Co, Ni, Zn, Cu) as effective electrocatalysts toward electrochemical hydrogen evolution reaction. *Int. J. Hydrogen Energy* **2022**, *47*, 20129–20137. [CrossRef]
3. Qureshi, F.; Yusuf, M.; Kamyab, H.; Vo, D.-V.N.; Chelliapan, S.; Joo, S.-W.; Vasseghian, Y. Latest eco-friendly avenues on hydrogen production towards a circular bioeconomy: Currents challenges, innovative insights, and future perspectives. *Renew. Sustain. Energy Rev.* **2022**, *168*, 112916. [CrossRef]
4. Manohar, A.; Vijayakanth, V.; Vattikuti, S.P.; Kim, K.H. Structural, BET and EPR properties of mixed zinc-manganese spinel ferrites nanoparticles for energy storage applications. *Ceram. Int.* **2023**, *49*, 19717–19727. [CrossRef]
5. Zhang, W.; Fu, Y.; Liu, W.; Lim, L.; Wang, X.; Yu, A. A general approach for fabricating 3D MFe_2O_4 (M = Mn, Ni, Cu, Co)/graphitic carbon nitride covalently functionalized nitrogen-doped graphene nanocomposites as advanced anodes for lithium-ion batteries. *Nano Energy* **2019**, *57*, 48–56. [CrossRef]
6. Zhang, X.; Liu, H.; Liang, C.; Ren, F.; Zhao, J.; Wang, T.; Zhong, R.; Zhang, D.; Zhu, H. Preparation of uniform and highly dispersed magnetic copper ferrite sub- micron sized particles regulated by short-chain surfactant with catechol structure: Dual-functional materials for supercapacitor and dye degradation. *J. Electroanal. Chem.* **2020**, *870*, 114199. [CrossRef]
7. Manohar, A.; Vijayakanth, V.; Vattikuti, S.P.; Kim, K.H. Synthesis and characterization of Mg^{2+} substituted $MnFe_2O_4$ nanoparticles for supercapacitor applications. *Ceram. Int.* **2022**, *48*, 30695–30703. [CrossRef]
8. Yadav, H.M.; Ghodake, G.S.; Kim, D.Y.; Ramesh, S.; Maile, N.C.; Lee, D.S.; Shinde, S.K. Nanorods to hexagonal nanosheets of CuO-doped manganese oxide nanostructures for higher electrochemical supercapacitor performance. *Colloids Surf. B Biointerfaces* **2019**, *184*, 110500. [CrossRef]
9. Tanuja, G.; Ganiger, S.K.; Shashidhar, S.; Preeti, R.; Patil, S.R.; Lagashetty, A. Solid state synthesis, characterization and biological evaluation of silver doped nanosized metal oxides. *Curr. Chem. Lett.* **2023**, *12*, 821–830. [CrossRef]
10. Barbosa, F.F.; de Oliveira Soares, J.; Miranda, M.O.; Torres, M.A.M.; Braga, T.P. Catalysis Application of Magnetic Ferrites and Hexaferrites. In *Handbook of Magnetic Hybrid Nanoalloys and Their Nanocomposites*; Springer International Publishing: Cham, Switzerland, 2022; pp. 1–42.
11. Khairy, M.; Bayoumy, W.A.; Selima, S.S.; Mousa, M.A. Studies on characterization, magnetic and electrochemical properties of nano-size pure and mixed ternary transition metal ferrites prepared by the auto-combustion method. *J. Mater. Res.* **2020**, *35*, 2652–2663. [CrossRef]
12. Deer, W.A.; Howie, R.A.; Zussman, J. *An Introduction to the Rock-Forming Minerals*; Scientific and Technology; Longman Scientific & Technical: London, UK, 1992.
13. Bogle, K.A.; Dhole, S.D.; Bhoraskar, V.N. Silver nanoparticles: Synthesis and size control by electron irradiation. *Nanotechnology* **2006**, *17*, 3204–3208. [CrossRef]
14. Gangopadhyay, P.; Kesavamoorthy, R.; Bera, S.; Magudapathy, P.; Nair, K.G.M.; Panigrahi, B.K.; Narasimhan, S.V. Optical Absorption and Photoluminescence Spectroscopy of the Growth of Silver Nanoparticles. *Phys. Rev. Lett.* **2005**, *94*, 047403. [CrossRef] [PubMed]
15. Hassanzadeh-Tabrizi, S.A.; Behbahanian, S.; Amighian, J. Synthesis and magnetic properties of $NiFe_{2-x}Sm_xO_4$ nanopowder. *Magn. Magn. Mater.* **2016**, *410*, 242–247. [CrossRef]
16. Aafiya; Abushad, M.; Arshad, M.; Naseem, S.; Ahmed, H.; Ansari, A.; Chakradhary, V.K.; Husain, S.; Khan, W. Synthesis and role of structural disorder on the optical, magnetic and dielectric properties of Zn doped $NiFe_2O_4$ nanoferrites. *J. Mol. Struct.* **2022**, *1253*, 132205. [CrossRef]
17. Dippong, T.; Levei, E.A.; Goga, F.; Petean, I.; Avram, A.; Cadar, O. The impact of polyol structure on the formation of $Zn_{0.6}Co_{0.4}Fe_2O_4$ spinel-based pigments. *J. Sol-Gel Sci. Technol.* **2019**, *92*, 736–744. [CrossRef]

18. Bhame, S.D.; Joy, P. Enhanced strain sensitivity in magnetostrictive spinel ferrite $Co_{1-x}Zn_xFe_2O_4$. *J. Magn. Magn. Mater.* **2018**, *447*, 150–154. [CrossRef]
19. Kaur, A.; Bhargava, G.K. Review paper on nickel-zinc nano ferrite. *Mater. Today Proc.* **2021**, *37*, 3082–3086. [CrossRef]
20. Pottker, W.E.; Ono, R.; Cobos, M.A.; Hernando, A.; Araujo, J.F.; Bruno, A.C.; Lourenço, S.A.; Longo, E.; La Porta, F.A. Influence of order-disorder effects on the magnetic and optical properties of $NiFe_2O_4$ nanoparticles. *Ceram. Int.* **2018**, *44*, 17290–17297. [CrossRef]
21. Hoghoghifard, S.; Moradi, M. Influence of annealing temperature on structural, magnetic, and dielectric properties of $NiFe_2O_4$ nanorods synthesized by simple hydrothermal method. *Ceram. Int.* **2022**, *48*, 17768–17775. [CrossRef]
22. Barvinschi, P.; Stefanescu, O.; Dippong, T.; Sorescu, S.; Stefanescu, M. $CoFe_2O_4/SiO_2$ nanocomposites by thermal decomposition of some complex combinations embedded in hybrid silica gels. *J. Therm. Anal. Calorim.* **2013**, *112*, 447–453. [CrossRef]
23. Luo, T.; Hou, X.; Liang, Q.; Zhang, G.; Chen, F.; Xia, Y.; Ru, Q.; Yao, L.; Wu, Y. The influence of manganese ions doping on nanosheet assembly $NiFe_2O_4$ for the removal of Congo red. *J. Alloys Compd.* **2018**, *763*, 771–780. [CrossRef]
24. Chakradhary, V.K.; Ansari, A.; Akhtar, M.J. Design, synthesis, and testing of high coercivity cobalt doped nickel ferrite nanoparticles for magnetic applications. *J. Magn. Magn. Mater.* **2019**, *469*, 674–680. [CrossRef]
25. Yan, M.F.; Johnson, D.W., Jr. Impurity-induced exaggerated grain growth in Mn-Zn Ferrites. *J. Am. Ceram. Soc.* **1978**, *61*, 342–349. [CrossRef]
26. El Nahrawy, A.M.; Hemdan, B.A.; Mansour, A.; Elzwawy, A.; Hammad, A.B.A. Integrated use of nickel cobalt aluminoferrite/Ni^{2+} nano-crystallites supported with SiO_2 for optomagnetic and biomedical applications. *Mater. Sci. Eng. B* **2021**, *274*, 115491. [CrossRef]
27. Sarker, M.; Yeasmin, M.; Al-Mamun, A.; Hoque, S.M.; Khan, M. Influence of Gd content on the structural, Raman spectroscopic and magnetic properties of $CoFe_2O_4$ nanoparticles synthesized by sol-gel route. *Ceram. Int.* **2022**, *48*, 33323–33331. [CrossRef]
28. More, G.S.; Shivhare, A.; Kaur, S.P.; Kumar, T.D.; Srivastava, R. Catalytic interplay of metal ions (Cu^{2+}, Ni^{2+}, and Fe^{2+}) in MFe_2O_4 inverse spinel catalysts for enhancing the activity and selectivity during selective transfer hydrogenation of furfural into 2-methylfuran. *Catal. Sci. Technol.* **2022**, *12*, 4857–4870. [CrossRef]
29. Paswan, S.K.; Pradhan, L.K.; Kumar, P.; Kumari, S.; Kar, M.; Kumar, L. Electrical transport properties of nanocrystalline and bulk nickel ferrite using complex impedance spectroscopy: A comparative study. *Phys. Scr.* **2022**, *97*, 095812. [CrossRef]
30. Manohar, A.; Vijayakanth, V.; Vattikuti, S.P.; Kim, K.H. Electrochemical investigation on nickel-doped spinel magnesium ferrite nanoparticles for supercapacitor applications. *Mater. Chem. Phys.* **2023**, *301*, 127601. [CrossRef]
31. Aakash; Nordblad, P.; Mohan, R.; Mukherjee, S. Structural, magnetic and hyperfine characterizations of nanocrystalline Zn-Cd doped nickel ferrites. *J. Magn. Magn. Mater.* **2017**, *441*, 710–717. [CrossRef]
32. Reddy, C.V.; Byon, C.; Narendra, B.; Dudem, B.; Shim, J.; Moon, S.J.; Vattikuti, S.V.P. Effect of calcination temperature on cobalt substituted cadmium ferrite nanoparticles. *J. Mater. Sci. Mater. Electron.* **2015**, *26*, 5078–5084. [CrossRef]
33. Dalawai, S.P.; Gadkari, A.B.; Vasambekar, P.N. Electrical switching in cadmium ferrite with different rare-earth ions (Sm^{3+}, Y^{3+}, and La^{3+}). *Rare Met.* **2015**, *34*, 133–136. [CrossRef]
34. Hajalilou, A.; Hashim, M.; Ebrahimi-Kahrizsangi, R.; Sarami, N. Influence of CaO and SiO_2 co-doping on the magnetic, electrical properties and microstructure of a Ni–Zn ferrite. *J. Phys. D Appl. Phys.* **2015**, *48*, 145001. [CrossRef]
35. Szczygieł, I.; Winiarska, K.; Bieńko, A.; Suracka, K.; Gaworska-Koniarek, D. The effect of the sol–gel autocombustion synthesis conditions on the Mn–Zn ferrite magnetic properties. *J. Alloys Compd.* **2014**, *604*, 1–7. [CrossRef]
36. Prabhakaran, T.; Hemalatha, J. Chemical control on the size and properties of nano $NiFe_2O_4$ synthesized by sol–gel autocombustion method. *Ceram. Int.* **2014**, *40*, 3315–3324. [CrossRef]
37. Rao, L.S.; Rao, T.V.; Naheed, S.; Rao, P.V. Structural and optical properties of zinc magnesium oxide nanoparticles synthesized by chemical co-precipitation. *Mater. Chem. Phys.* **2018**, *203*, 133–140. [CrossRef]
38. Ma, C.; Xu, F.; Zhu, Z.; Yang, H.; Nong, P.; Kang, Z.; Tang, S.; Zhang, L.; Zhu, Y. Dissolution and Solubility of the Calcite–Otavite Solid Solutions $[(Ca_{1-x}Cd_x)CO_3]$ at 25 °C. *Minerals* **2022**, *12*, 756. [CrossRef]
39. Mashekova, A.; Baltash, Y.; Yegamkulov, M.; Trussov, I.; Bakenov, Z.; Mukanova, A. Polycationic doping of the LATP ceramic electrolyte for Li-ion batteries. *RSC Adv.* **2022**, *12*, 29595–29601. [CrossRef] [PubMed]
40. Umapathy, G.; Senguttuvan, G.; Berchmans, L.J.; Sivakumar, V.; Jegatheesan, P. Influence of cerium substitution on structural, magnetic and dielectric properties of nanocrystalline Ni–Zn ferrites synthesized by combustion method. *J. Mater. Sci. Mater. Electron.* **2017**, *28*, 17505–17515. [CrossRef]
41. Lai, X.; Li, J.; Korgel, B.A.; Dong, Z.; Li, Z.; Su, F.; Du, J.; Wang, D. General synthesis and gas-sensing properties of multiple-shell metal oxide hollow microspheres. *Angew. Chem. Int. Ed.* **2011**, *12*, 2738–2741. [CrossRef]
42. Pahwa, C.; Narang, S.B.; Sharma, P. Composition dependent magnetic and microwave properties of exchange-coupled hard/soft nanocomposite ferrite. *J. Alloys Compd.* **2020**, *815*, 152391. [CrossRef]
43. ur Rehman, A.; Ahmad, M.; Hassan, S.; Hussain, S.Q.; Iqbal, M.W.; Ali, H.E. Ba substituted SrFe2O4 ($SrBa_{0.3}Fe_{1.7}O_4$) for the removal of fluoride ions (F^{-1}) from the drinking water. *Mater. Chem. Phys.* **2023**, *295*, 127165. [CrossRef]
44. Rehman, A.U.; Shaukat, S.F.; Haidyrah, A.S.; Akhtar, M.N.; Ahmad, M. Synthesis and investigations of structural, magnetic and dielectric properties of Cr-substituted W-type Hexaferrites for high frequency applications. *J. Electroceram.* **2021**, *46*, 93–106. [CrossRef]

45. Ahmad, M.; Ali, R.; Rehman, A.U.; Ali, A.; Sultana, I.; Ali, I.; Asif, M. Insight into the Structural, Electrical, and Magnetic Properties of Al-Substituted $BiFeO_3$ Synthesised by the Sol–Gel Method. *Z. Naturforschung A* **2020**, *75*, 249–256. [CrossRef]
46. Ahmad, M.; Grössinger, R.; Ali, I.; Ahmad, I.; Rana, M. Synthesis and characterization of Al-substituted W-type hexagonal ferrites for high frequency applications. *J. Alloys Compd.* **2013**, *577*, 382–388. [CrossRef]
47. Qin, X.; Cheng, Y.; Zhou, K.; Huang, S.; Hui, X. Microwave absorbing properties of W-type hexaferrite $Ba(MnZn)_xCo_{2(1-x)}Fe_{16}O_{27}$. *J. Mater. Sci. Chem. Eng.* **2013**, *1*, 8–13.
48. Wang, S.X.; Sun, N.X.; Yamaguchi, M.; Yabukami, S. Properties of a new soft magnetic material. *Nature* **2000**, *407*, 150–151. [CrossRef]
49. Almessiere, M.; Slimani, Y.; Korkmaz, A.; Guner, S.; Sertkol, M.; Shirsath, S.E.; Baykal, A. Structural, optical and magnetic properties of Tm^{3+} substituted cobalt spinel ferrites synthesized via sonochemical approach. *Ultrason. Sonochem.* **2019**, *54*, 1–10. [CrossRef]
50. Akhtar, M.N.; Khan, M.A. Structural, physical and magnetic evaluations of Ce-Zn substituted $SrCo_2$ W-type hexaferrites prepared via sol gel auto combustion route. *Ceram. Int.* **2018**, *44*, 12921–12928. [CrossRef]
51. van der Zaag, P.J.; van der Valk, P.J.; Rekveldt, M.T. A domain size effect in the magnetic hysteresis of NiZn-ferrites. *Appl. Phys. Lett.* **1996**, *69*, 2927–2929. [CrossRef]
52. Maaz, K.; Mumtaz, A.; Hasanain, S.; Bertino, M. Temperature dependent coercivity and magnetization of nickel ferrite nanoparticles. *J. Magn. Magn. Mater.* **2010**, *322*, 2199–2202. [CrossRef]
53. Mukherjee, S.; Sarkar, K. Effect of Nickel and Cobalt Doping on Nano Bismuth Ferrite Prepared by the Chemical Route. *Interceram-Int. Ceram. Rev.* **2015**, *64*, 38–43. [CrossRef]
54. Kumar, N.; Archana; Singh, R.K.; Kumar, V.; Das, S.B. Tuning in structural, optoelectronic, magnetic and ferroelectric properties of $NiFe_2O_4$ ceramics engineering nanomaterials by substitution of rare earth element, Pr^{3+} prepared by sol–gel method. *J. Mater. Sci. Mater. Electron.* **2022**, *33*, 6131–6149. [CrossRef]
55. Iqbal, S.; Bibi, I.; Majid, F.; Jilani, K.; Kamal, S.; Iqbal, M.; Ata, S.; Nazar, N.; Albalawi, H.; Alwadai, N. The electrochemical, dielectric, and ferroelectric properties of Gd and Fe doped $LaNiO_3$ with an efficient solar-light driven catalytic activity to oxidize malachite green dye. *J. Colloid Interface Sci.* **2022**, *607*, 568–583. [CrossRef] [PubMed]
56. Luqman, M.; Shazaib, R.; Raza, A.; Khan, M.A.; Shar, M.; Ramay, S.M.; Riaz, S.; Atiq, S. Simultaneous existence of magnetic and ferroelectric orders in bi-phase composites for multiferroic applications. *J. Magn. Magn. Mater.* **2023**, *587*, 171361. [CrossRef]

Disclaimer/Publisher's Note: The statements, opinions and data contained in all publications are solely those of the individual author(s) and contributor(s) and not of MDPI and/or the editor(s). MDPI and/or the editor(s) disclaim responsibility for any injury to people or property resulting from any ideas, methods, instructions or products referred to in the content.